

Mass-loaded magnetic explosions in the context of Magnetar Giant Flares and Fast Radio Bursts

K.N. Gourgouliatos

Laboratory of Universe Sciences, Department of Physics, University of Patras, Patras, Rio, 26504, Greece
e-mail: kngourg@upatras.gr

Received —; accepted —

ABSTRACT

Context. Magnetar flares are highly energetic and rare events where intense X and γ -ray emission is released from strongly magnetised neutron stars and are accompanied by mass ejection from the neutron star. Fast radio bursts are short and intense pulses of coherent radio emission. Their large dispersion measures support an extragalactic origin. While their exact origin still remains elusive, a substantial number of models associates them with strong magnetic field and high-energy relativistic plasma found in the vicinity of magnetars. There is growing evidence that some fast radio bursts are associated to flare-type events from magnetars.

Aims. We aim to provide a set of configurations describing a relativistic, spherical, mass-loaded, magnetic explosion. We proceed by solving the equations of relativistic magnetohydrodynamics, for a system that expands while maintaining its internal equilibrium.

Methods. We employ a semi-analytical approach for the solution of the equations of relativistic magnetohydrodynamics. We assume self-similarity in time and radius, axial symmetry, and separation of variables in the spherical and polar angle coordinate. This allows the reduction of the problem to the solution of a set of ordinary differential equations.

Results. We find the interdependent relation between pressure, mass density, Lorentz factor, and magnetic field that determines the detailed properties of the solutions. There exists a dichotomy of solutions that correspond to higher and lower density and thermal pressure compared to the external one. For stronger toroidal magnetic fields the maximum expansion velocity, permitted, becomes smaller compared to weaker toroidal fields. For given ratio of toroidal to poloidal field, the inclusion of pressure and mass density leads to either higher expansion velocity if the density and pressure are lower in the regions where the magnetic flux is higher; whereas, if the pressure and mass density are higher in the regions where the magnetic flux is higher, the expansion velocity is smaller.

Conclusions. The classes of these solutions can be applied to magnetar giant flares and fast radio bursts. The ones corresponding to overdensities and higher pressure can be associated to magnetar flares, whereas the ones corresponding to underdensities can be relevant to fast radio bursts corresponding to magnetically dominated events with low mass loading.

Key words. Neutron Stars – Magnetars – FRBs, MHD

1. Introduction

Magnetars are hosts of highly energetic events, releasing radiation in X-ray and γ -rays. The most energetic of these events are giant flares, that release an isotropic luminosity up to 10^{47} erg/s (Hurley et al. 1999; Palmer et al. 2005; Hurley et al. 2005). Such events have been observed from extra-galactic sources (Beniamini et al. 2025; Trigg et al. 2025) and have been associated to strong magnetised explosions (Thompson & Duncan 1995) originating from magnetars where a major reconfiguration of the global magnetic field has occurred (Lyutikov 2006). Magnetar flares also are loaded with mass entrained from the crust and the interior of the neutron star (Frail et al. 1999; Demidov & Lyubarsky 2023; Patel et al. 2025). Thus, a complete view of giant flares, requires the modelling of a mass-loaded magnetised explosion, reaching relativistic velocities.

The collection of an ample sample of fast radio bursts (FRBs), which are millisecond-duration transients of extragalactic origin, allows to explore their diverse phenomenology, which point to coherent emission from compact astrophysical sources (Lorimer et al. 2007; Petroff et al. 2019). Since their discovery, FRBs have challenged theoretical models, demanding mechanisms capable of releasing up to 10^{40} erg in radio waves over millisecond timescales, often with repetition, polarization, and spectral properties indicative of strong magnetized environments

(Marcote et al. 2020). The growing evidence linking at least a subset of FRBs to magnetars — particularly the association of FRB 200428 with the Galactic magnetar SGR 1935+2154 (Bochenek et al. 2020; CHIME/FRB Collaboration et al. 2020) — has reinforced the idea that magnetic energy release in highly magnetized neutron stars can power these events.

Despite this association, the detailed physics linking magnetic activity to FRB emission remains uncertain. Proposed mechanisms span a broad range, from magnetospheric reconnection and crustal cracking to relativistic shocks in magnetar winds (e.g. Lyubarsky 2014; Beloborodov 2017; Metzger et al. 2019). Most models assume magnetically dominated outflows capable of generating coherent radio emission through synchrotron maser, shocks or antenna processes, and possibly a combination of those (Lyubarsky 2021). Theoretical and observational developments suggest that magnetar magnetospheres may often be mass-loaded by plasma ejected during starquakes, bursts, or fallback episodes (Thompson & Duncan 1995; Wadiasingh & Timokhin 2019; Yuan et al. 2020). Moreover, the connection between magnetar bursts and flares and FRBs that has been confirmed recently (Bochenek et al. 2020; Tavani et al. 2021; Beniamini et al. 2025), stresses the necessity to consider mass loaded magnetic detonations that may be related to an event originating from the neutron star interior and propagating to the magneto-

sphere (Bransgrove et al. 2025). The presence of dense plasma in a strongly magnetised environment may substantially modify the dynamics of magnetic explosions, their ability to accelerate particles, and the conditions for coherent emission.

In this work, we explore mass-loaded magnetic explosions as potential origins of magnetar giant flares and FRBs. Using simplified relativistic magnetohydrodynamic (MHD) models, we examine how the interplay between magnetic field, plasma mass loading, and self-similar expansion shapes the energetics and temporal properties of such events. The proposed structures can provide an appropriate environment that can lead to the generation of short, intense events with energetics and timescales consistent with observed FRBs.

To model the coupled evolution of the magnetic field and plasma during these explosive events, we adopt the formalism developed in Gourgouliatos & Vlahakis (2010), which provides a self-consistent description of self-similar, co-expanding magnetized outflows. In this framework, the plasma and magnetic field evolve together under a homologous (Hubble-type) expansion, preserving the topology of the magnetic field while allowing for a time-dependent redistribution of electro-magnetic and kinetic energy.

The underlying concept traces back to the Prendergast (2005) family of self-similar, uniformly-expanding, axisymmetric magnetic equilibria. These equilibria, later extended by Gourgouliatos & Lynden-Bell (2008) to include non-linear poloidal currents and toroidal fields, demonstrated that magnetic structures can expand coherently, a key insight for modelling transient magnetic explosions in compact objects. Building on this foundation, Gourgouliatos & Vlahakis (2010) formulated a relativistic configuration that couples the magnetic and velocity fields in a co-expanding MHD flow, enabling analytical and numerical exploration of outflows that evolve self-similarly while conserving magnetic helicity and flux. In these models the field originates from an appropriately twisted dipolar located at the origin. Due to the singularity at the origin the field is studied beyond an inner radius, that serves as a lower boundary condition.

More recently, Barkov et al. (2022) applied similar ideas for numerical solutions of magnetic explosions in magnetically dominated and mass-loaded environments, demonstrating how magnetic energy release can drive relativistic outflows and shocks capable of producing bright, short-duration transients. In the same work, analytical solutions of force-free magnetic fields, in the absence of thermal pressure and inertia forces, were presented. These solutions do not diverge at the origin. It was found that the maximum expansion rate that can be attained by the expanding structure depends on the amount of twist of the magnetic field, with highly twisted magnetic fields not being able to expand at highly relativistic rates. In the absence of any thermal pressure and inertia, the pressure on the surface of the boundary of the spherical explosion is highly anisotropic due to the magnetic field structure, i.e. in the dipole case it is maximum on the equator and becomes zero on the axis of symmetry. Such a structure if embedded within a uniform pressure environment it will expand side-ways on the equator and will form a highly anisotropic explosion, while it will lose its internal equilibrium and coherence. The inclusion of mass density and thermal pressure leads to configurations in the form of large-scale plasmoids whose surface pressure, including the electromagnetic term is more isotropic and under certain conditions it can even become completely isotropic, with the surface magnetic field completely vanishing, as has been shown in the non-relativistic approach (Gourgouliatos et al. 2010). Such structures continue their uniform expansion if they are situated in a uniform density medium

and maintain their internal equilibrium (Gourgouliatos & Lyutikov 2012).

In the present work, we extend these ideas by embedding mass-loaded magnetic explosions within the relativistically expanding self-similar MHD formalism of Gourgouliatos & Vlahakis (2010). This allows us to follow consistently the co-evolution of magnetic fields and plasma during an explosive expansion, explore the interplay between magnetic field strength, mass and pressure and its effect on the expansion rate. This, will allow the identification of the physical conditions under which such events can generate coherent radio emission with energetics and timescales comparable to magnetar flares and FRBs.

This paper is organized as follows. In section 2, we outline the physical and mathematical framework for mass-loaded magnetic explosions and describe the key ingredients of our model. Section 3 presents the solutions and the exploration of the parameter space. The results are discussed in section 4, focusing on energy release, plasma dynamics, and physical properties of the solution. In section 5, we discuss the implications for astrophysical sources with main focus on magnetar bursts and FRBs. We conclude in section 6 and outline the limitations of the current model and the prospects for future work.

2. Mathematical Formulation

Consider a fluid of rest mass density ρ , pressure p containing a magnetic field \mathbf{B} . The electric and magnetic field obey Maxwell's equations:

$$\nabla \cdot \mathbf{B} = 0, \quad (1)$$

$$\nabla \cdot \mathbf{E} = \frac{4\pi}{c} j^0, \quad (2)$$

$$\nabla \times \mathbf{E} = -\frac{1}{c} \frac{\partial \mathbf{B}}{\partial t}, \quad (3)$$

$$\nabla \times \mathbf{B} = \frac{1}{c} \frac{\partial \mathbf{E}}{\partial t} + \frac{4\pi}{c} \mathbf{j}, \quad (4)$$

where j^0 is the electric charge density, \mathbf{j} the electric current density and c the speed of light. We will further consider ideal-MHD, thus there is no electric field in the co-moving frame of the fluid. For an observer who sees the fluid moving at velocity \mathbf{v} , normalised to the speed of light, Ohm's law becomes:

$$\mathbf{E} = -\mathbf{v} \times \mathbf{B}. \quad (5)$$

The continuity equation reads:

$$\partial_t(\Gamma\rho) + \nabla \cdot (\Gamma\rho\mathbf{v}) = 0, \quad (6)$$

where Γ is the Lorentz factor:

$$\Gamma = \frac{1}{\sqrt{1 - v^2}} \quad (7)$$

The momentum equation is:

$$\Gamma\rho(\partial_t + c\mathbf{v} \cdot \nabla)(\xi\Gamma\mathbf{v}) + \nabla p - \frac{j^0\mathbf{E} + \mathbf{j} \times \mathbf{B}}{c} = \mathbf{0}, \quad (8)$$

where p is the pressure and the relativistic specific enthalpy is given by the following expression:

$$\xi = 1 + \frac{\gamma}{1 - \gamma} \frac{p}{\rho c^2}, \quad (9)$$

where γ is the ratio of the specific heats. Furthermore, the entropy equation reads:

$$(\partial_t + c\mathbf{v} \cdot \nabla) \left(\frac{p}{\rho^\gamma} \right) = 0. \quad (10)$$

In what follows we assume a relativistic degenerate gas where $\gamma = 4/3$. We will further consider spherical coordinates (r, θ, ϕ) and prescribe a velocity given by the following expression:

$$\mathbf{v} = \frac{r}{ct} \hat{\mathbf{r}}. \quad (11)$$

This velocity corresponds to uniform expansion from the centre. Thus, each fluid element moves at constant velocity without any acceleration and the system remains implicitly at force balance.

It is possible to find self-similar, separable solutions using as main variables the polar angle θ and the expansion velocity v . The full details of this procedure are shown Prendergast (2005); Gourgouliatos & Lynden-Bell (2008); Gourgouliatos & Vlahakis (2010), here we summarise the basic steps for clarity and consistency.

We express the magnetic field in terms of two functions: one related to the poloidal field $\Psi(\theta, v)$ and another to the toroidal $T(\theta, v)$:

$$\mathbf{B} = \frac{1}{2\pi r^2 \sin \theta} \left(\partial_\theta \Psi \hat{\mathbf{r}} - v \partial_v \Psi \hat{\theta} + T \hat{\phi} \right). \quad (12)$$

Combining Ohm's law, equation (5), with the momentum equation (8), and taking the toroidal component, one deduces that the poloidal and toroidal functions are related to each other through the following expression:

$$T = \Gamma^2 v H(\Psi), \quad (13)$$

where $H(\Psi)$ is an arbitrary function of Ψ .

The pressure and the density are related through the entropy equation (10), which is satisfied for:

$$\frac{p}{r^{4/3}} = Q(v, \theta), \quad (14)$$

where $Q(v, \theta)$ is an arbitrary function of v and θ . Upon integration of the continuity equation (6), we obtain that:

$$\rho = \tilde{\rho}(v, \theta) \frac{\Gamma^3 v^3}{r^3}, \quad (15)$$

and combining this with equation (14), we find that the pressure has the following form:

$$p = \tilde{p}(v, \theta) \frac{\Gamma^4 v^4}{r^4}, \quad (16)$$

where the quantities $Q, \tilde{p}, \tilde{\rho}$, all depending on the separation variables v and θ , related to each other through the following expression:

$$Q = \frac{\tilde{p}}{\tilde{\rho}^{4/3}}. \quad (17)$$

Next, we evaluate the current and charge densities, through Maxwell's equations (2) and (4) and substitute them into the momentum equation (8). We find that $\tilde{p} = \tilde{p}(\Psi)$ and that the system should satisfy the following equation:

$$\begin{aligned} v^2 \frac{\partial^2 \Psi}{\partial v^2} - \frac{2v^2}{1-v^2} \frac{\partial \Psi}{\partial v} + \frac{\sin \theta}{1-v^2} \frac{\partial}{\partial \theta} \left(\frac{1}{\sin \theta} \frac{\partial \Psi}{\partial \theta} \right) \\ + \frac{v^2}{(1-v^2)^2} H \frac{dH}{d\Psi} + 16\pi^3 \sin^2 \theta \frac{v^4}{(1-v^2)^3} \frac{d\tilde{p}}{d\Psi} = 0 \end{aligned} \quad (18)$$

Separable solutions in v and θ are feasible under the following assumptions:

$$\Psi = g(v) \sin^2 \theta, \quad H \frac{dH}{d\Psi} = c_0 \Psi, \quad \frac{d\tilde{p}}{d\Psi} = \frac{c_1}{16\pi^3}. \quad (19)$$

Upon integration, and considering the fact the B_ϕ component of the field must remain finite:

$$H(\Psi) = \pm \sqrt{c_0} g \sin^2 \theta, \quad (20)$$

with c_0 a non-negative constant, which governs the intensity of the toroidal field or equivalently the poloidal current. The pressure term becomes:

$$\tilde{p} = \tilde{p}_0 + \frac{c_1}{16\pi^3} g \sin^2 \theta. \quad (21)$$

In the above expression \tilde{p}_0 is the pressure on the axis and the spherical surface of the plasmoid; and it has to be a non-zero constant. There is no constraint on the sign of c_1 , however, the combination of \tilde{p}_0 and c_1 must ensure that \tilde{p} remains non-negative throughout the solution.

Finally, substituting the expressions from equation (19) into equation (18) we obtain an ordinary differential equation for $g(v)$:

$$v^2 g'' - \frac{2v^3 g'}{1-v^2} - \frac{2g}{1-v^2} + \frac{c_0 v^2 g}{(1-v^2)^2} + \frac{c_1 v^4}{(1-v^2)^3} = 0. \quad (22)$$

The solution of the above equation will provide the radial structure of the configuration.

3. Solutions

By taking the limit of $v \ll 1$ we find that there are two main classes of solutions of equation (22). A class where $g \propto v^{-1}$, leading to solutions that reduce to a magnetic dipole near the origin, and a class where $g \propto v^2$ where the field near the centre is approximately uniform. While the former case was explored in detail in Gourgouliatos & Vlahakis (2010), the latter has not been studied. In this work we will focus on the latter class of solutions that are not singular at the origin by exploring appropriate combinations of the main parameters c_0 and c_1 .

The equation does not permit general analytical solutions and we shall proceed with a numerical solution. Given the singularities at $v = 0$ and $v = 1$, we integrate within an interval $v \in [v_{min}, v_{max}]$, where $v_{min} = 10^{-3}$ and $v_{max} < 1$. We set $g(v_{min})' = 0$, and $g(v_{min}) = g_0$, we choose g_0 , so that the maximum value of g is set to unity. This is straightforward for the homogeneous version of the equation with $c_1 = 0$, as a simple division with the maximum value of a trial solution with arbitrary g_0 leads to a normalised solution. However, in the non-homogeneous case ($c_1 \neq 0$) it requires an iterative processes as simple division of the function does not lead to a solution. Thus, we repeat the process by dividing g_0 by the maximum value of the solution and integrating, until convergence. We use a tolerance limit of 10^{-4} for the normalisation and we typically find that the solution converges to a normalised form after less than 100 iterations. For the integration of the ordinary differential equation we used the Runge-Kutta-Fehlberg method, applying the built-in routines of numpy and scipy in python (Harris et al. 2020; Virtanen et al. 2020).

The results of the integration for $c_1 = 0$ and various values of c_0 , ranging from 1 to 100 are shown in Figure 1, which are fully consistent with the analytical solutions reported in Barkov et al. (2022), with the note that the value of α there corresponds to $\sqrt{c_0}$ in this work. It can be seen clearly that by increasing the value of c_0 the maximum velocity attained by the expanding field becomes smaller. This velocity corresponds to the first root, beyond the origin $v = 0$, as $g(0) = 0$, of the function $g(v_0) = 0$. Thus, by increasing the ratio of the poloidal current over the

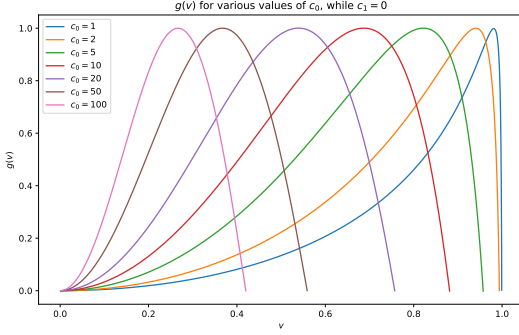


Fig. 1. The Z-family solutions for $g(v)$, for various values of c_0 while $c_1 = 0$.

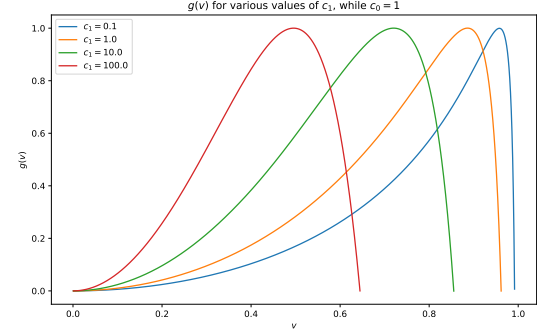


Fig. 2. Characteristic P-family solutions of $g(v)$ various values of c_1 , while keeping $c_0 = 1$.

poloidal field, or equivalently the ratio of the toroidal field over the poloidal field, the maximum expansion velocity is smaller. We note that beyond the v_0 the solutions becomes oscillatory, with the flux taking negative and positive values. However, this part of the solution is completely disconnected from the inner part, both in terms of the poloidal and the toroidal fields, thus no field lines from the central part are connected to the outer ones. Thus we halt the integration at v_0 . These solutions are denoted as Z-type solutions, as the pressure and density are zero.

Next, we have explored solutions with non-zero values of c_1 . Due to the large number of combinations, we have decided to keep the toroidal field parameter constant ($c_0 = 1$) and then explore positive values of c_1 , ranging from 0.1 to 100, with the results shown in Figure 2. The inclusion of pressure and density leads to a structure that is less extended in the velocity space, reaching a smaller maximum velocity compared to the $c_1 = 0$ case. We have denoted these solutions as P-type solutions, as the pressure and density increase with increasing magnetic flux function.

Finally, it is possible to explore negative values of c_1 . These cases correspond to plasmoids where the pressure decreases as the magnetic flux function increases. Despite this negative relation, the freedom of an additive constant \tilde{p}_0 in equation (21) prevents from negative values of the pressure and the density. These solutions have the remarkable property, that for an appropriate combination of c_0 and c_1 , not only the flux function reaches 0 at v_0 but also its derivative becomes zero there thus: $g'(v_0) = 0$, as shown in Figure 3. This has the important consequence that all three components the magnetic field are zero on the surface of the sphere. We note that if the values of c_1 are smaller algebraically than the ones corresponding to the zero derivative on the boundary, the solutions become unphysical with the field lines not closing but increasing infinitely. The resulting structures correspond to underdensities, where the drop of thermal plasma pressure and mass density within the sphere is compensated by the magnetic and electric field pressure and tension. We have denoted these as N-type solutions as in these solutions the density and pressure decrease with increasing flux function.

The parameters provided in table 1 were employed for the three families of solutions: $c_1 = 0$ Z-models, where there is no mass or thermal pressure, $c_1 > 0$ P-models, where there is mass and pressure varying with the same sign of the flux function, and $c_1 < 0$ N-models, where, in addition to the negative sign of c_1 , the derivative of g at v_0 vanishes.

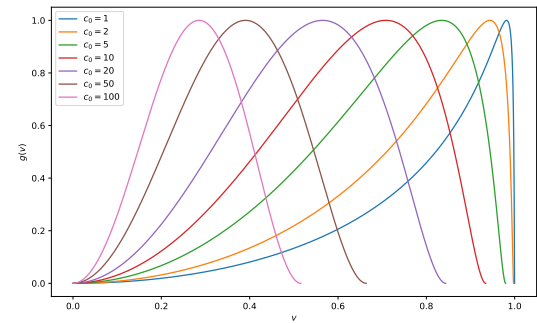


Fig. 3. The N-family of solutions showing $g(v)$, for various values of c_0 and negative c_1 , so that the derivative is zero at the maximum velocity.

4. Discussion

4.1. General properties of the solutions

Below we present a description of the main characteristics of the solutions depending on the values of the parameters used.

For all solutions, smaller values of c_0 lead to v_0 that approaches unity, thus the system becomes more relativistic. This implies that the more twisted the solution is, or equivalently if the poloidal current is higher, the plasmoid is contained within a smaller sphere. This property is related to the fact that by assuming a constant c_0 a particular length-scale is introduced. In this case the units of $\sqrt{c_0}$ are inversely proportional to length. Consequently, by increasing c_0 this length-scale becomes smaller. This is consistent with the well-known non-relativistic, linear force-free axisymmetric solutions in spherical geometry (Chandrasekhar & Kendall 1957) whose radius shifts to smaller values for larger toroidal-to-poloidal magnetic field ratio. This property is well-preserved and reflected on its relativistic analogue.

Regarding the surface terms, in Z and P solutions, there exists a non-vanishing meridional magnetic field on the surface $v = v_0$. Because of this magnetic field discontinuity an azimuthal electric current sheet flows on the surface of the plasmoid. Moreover, there also exists a volume electric charge, due to the divergence of the meridional component of the electric field. Following the convention of a positive value for the flux function, the charge is positive in the northern hemisphere and negative in the southern one. While this structure is in equilibrium at its interior, on its surface the magnetic pressure is anisotropic, stronger at the equator and weaker at the poles. Therefore, if it is embedded within a medium of uniform pressure, it is expected to expand on

Table 1. Solution properties: The columns represent the solution number, parameters c_0 , c_1 , the root of the solution v_0 and the corresponding Lorentz number Γ_0 , the magnetic field energy E_{mag} , the electric field energy E_{el} , the work of the pressure W and the mass M enclosed in the solution. The units of the various energy terms (E_{mag} , E_{el} and W) are in units of 10^{45} erg and the mass in units of 1.8×10^{26} g, under the assumption of a sphere of were $v = 1$, corresponds to a radius of 1km the magnetic flux g is normalised to 10^{25} G cm 2 .

Model	c_0	c_1	v_0	Γ_0	E_{mag}	E_{el}	W	M
Z1	1	0	0.9992	25.01	17.59	17.54	0	0
Z2	2	0	0.9939	9.07	1.018	0.9730	0	0
Z3	5	0	0.9573	3.46	0.2691	0.1998	0	0
Z4	10	0	0.8812	2.12	0.2004	0.1012	0	0
Z5	20	0	0.7571	1.53	0.2020	0.06043	0	0
Z6	50	0	0.5589	1.21	0.2598	0.03446	0	0
Z7	100	0	0.4201	1.10	0.3431	0.02354	0	0
P1	1	0.1	0.9918	7.82	1.742	1.693	0.02989	0.07039
P2	1	0.2	0.9870	6.22	1.012	0.9656	0.03759	0.08894
P3	1	0.5	0.9758	4.57	0.5457	0.4988	0.04932	0.1170
P4	1	1	0.9617	3.62	0.3654	0.3166	0.05971	0.1406
P5	1	2	0.9407	2.95	0.2614	0.2094	0.07180	0.1657
P6	1	5	0.8990	2.28	0.1872	0.1286	0.09086	0.1990
P7	1	10	0.8553	1.93	0.1593	0.09345	0.1085	0.2236
P8	1	20	0.8008	1.67	0.1445	0.06976	0.1292	0.2458
P9	1	50	0.7154	1.43	0.1392	0.04921	0.1628	0.2711
P10	1	100	0.6446	1.31	0.1435	0.03880	0.1937	0.2865
N1	1	-0.00135	0.9997	40.83	0.8867	0.8641	0.03083	0.02894
N2	2	-0.00170	0.9974	13.88	0.5897	0.5504	0.03353	0.05305
N3	5	-0.252	0.9779	4.78	0.2631	0.1970	0.05370	0.1107
N4	10	-1.448	0.9342	2.80	0.2024	0.1065	0.07718	0.1654
N5	20	-7.084	0.8434	1.86	0.2035	0.06541	0.1108	0.2194
N6	50	-50.45	0.6628	1.34	0.2592	0.03796	0.1767	0.2732
N7	100	-211.3	0.5135	1.17	0.3407	0.02609	0.2509	0.2983

the equatorial direction, while the presence of the surface current may trigger resistive instabilities and lead to reconnection on a layer that is propagating relativistically.

Considering the solutions with $c_1 > 0$, we find that higher values of c_1 lead to plasmoids with smaller v_0 . This is due to the inclusion of extra pressure and density that prevent the system from extending to a v_0 as high as in the purely electromagnetic case ($c_1 = 0$). The overall structure has similar characteristics to the previous solution, regarding the surface azimuthal current sheet and pressure profile and it be prone to similar instabilities.

Solutions of the N family, with $c_1 < 0$ lead to different qualitative properties. In general choosing a negative c_1 leads to v_0 closer to unity compared to the solutions with zero or positive c_1 and the same c_0 . Below a critical value of c_1 , the solution has no roots, thus becoming unphysical. In the N-class of solutions we have determined these critical values for various choices of c_0 . The solutions corresponding to these critical values have the remarkable property that at v_0 , not only the function g is zero but also its derivative vanishes. This implies that all three components of the magnetic field, and both components of the electric field are zero on the spherical surface defined by $v = v_0$. Because of this, there is no anisotropy nor a surface current due to the meridional component. Thus, if spherical plasmoids obeying these solutions are embedded within a medium of uniform pressure the system can maintain its equilibrium, as opposed to structures corresponding to the other families of solutions. Moreover, the lack of surface current sheets makes less likely the appearance of current driven instabilities.

4.2. Physical Quantities

Based on these solutions it is possible to calculate the corresponding physical quantities arising from these calculations. In what follows we focus on the electromagnetic field energy, the mass of the sphere, the work of the thermal pressure and the temperature of the plasmoid. A set of characteristic configurations and the corresponding physical properties are shown in Figures 4 and 5.

4.2.1. Electromagnetic Field

The electric and magnetic field are given from equations (5) and (12) with appropriate substitution of the solutions and the velocity profile. The electromagnetic field is contained within a sphere in the v -space. The poloidal field is approximately uniform close to the axis, and closes within a expanding sphere of radius $r_0 = cv_0 t$. The B_ϕ field peaks at the equatorial plane. However this peak does not coincide with the maximum of the flux function Ψ , which corresponds to the null point of the closed poloidal loops, Figures 4 and 5 panels a and e. This is due to the fact that the B_ϕ is proportional to Ψ , but is also multiplied by a factor $\frac{v^2}{r^2}$, which for the highly relativistic case dominates and pushes the maximum to more distant radii. Therefore, in the highly relativistic case, a thin layer containing a toroidal field expanding relativistically is expected, while in the non-relativistic case $v_0 \ll 1$ the toroidal field is contained closer to the centre.

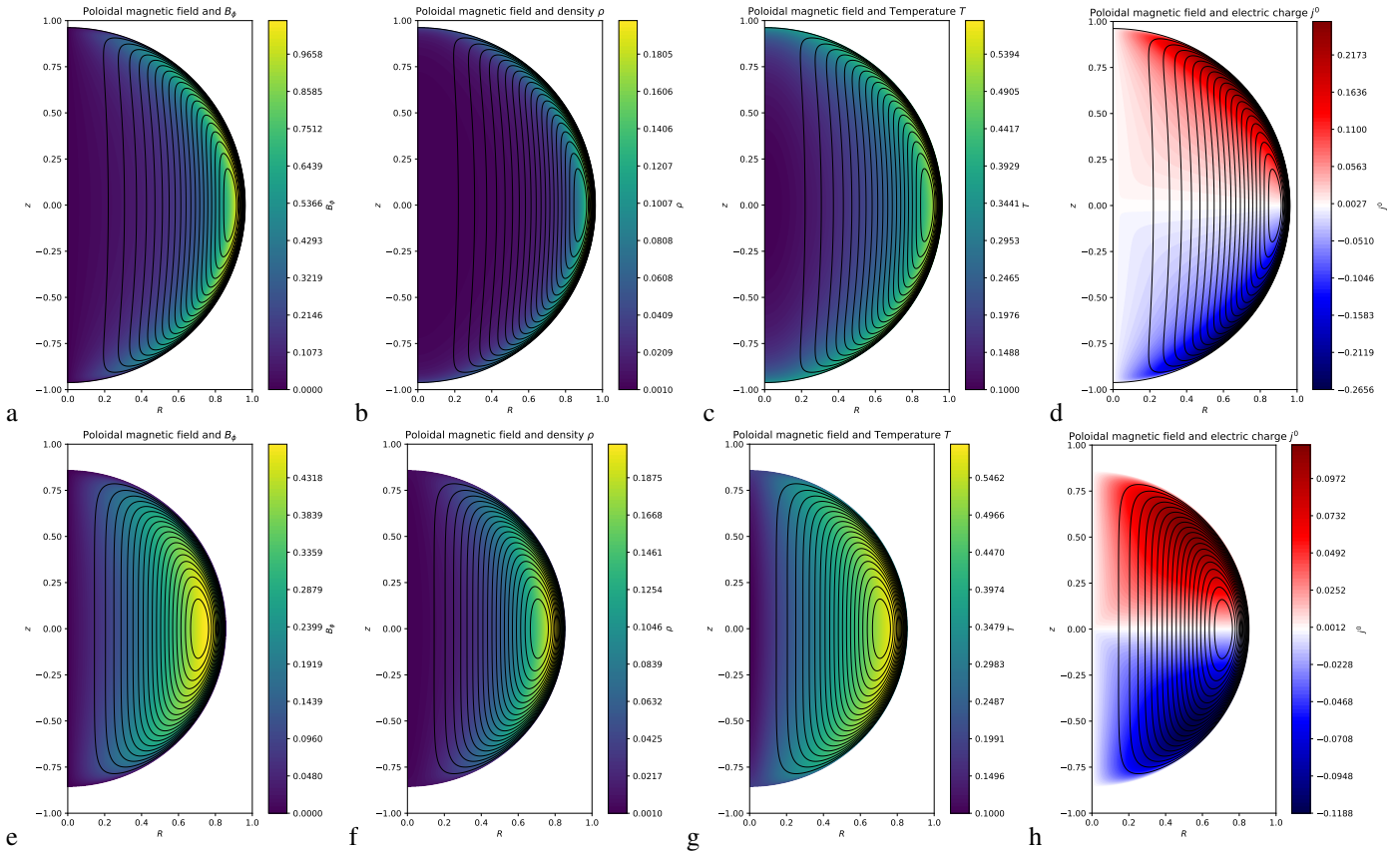


Fig. 4. Contour plots of the solutions with $c_0 = 1$ and $c_1 = 1$ (top row); and $c_0 = 1$ and $c_1 = 10$ (bottom row). The black contours correspond to the poloidal magnetic field lines, while in colour is plotted: the B_ϕ component of the magnetic field (panels a, e), the rest mass density ρ (panels b and f), the temperature T (panels c and g); and the electric charge density j^0 (panels d and h). The solution remains invariant in the v -space, here we present a snapshot at some time t , so that $r = 1$ corresponds to $v = 1$.

We can then calculate the energy of the electric and the magnetic field:

$$\begin{aligned}
 E_{mag} &= \frac{2\pi}{8\pi} \int_0^\pi \int_0^R \frac{1}{(2\pi r^2 \sin \theta)^2} \left[(\partial_\theta \Psi)^2 + \right. \\
 &+ (v \partial_v \Psi)^2 + \left(\Gamma^2 v \sqrt{c_0} \Psi \right)^2 \left. \right] r^2 \sin \theta dr d\theta \\
 &= \frac{1}{16\pi c t} \int_0^\pi \int_0^{v_0} \frac{1}{v^2 \sin^2 \theta} \left[(\partial_\theta \Psi)^2 + \right. \\
 &+ (v \partial_v \Psi)^2 + \left. \left(\Gamma^2 v \sqrt{c_0} \Psi \right)^2 \right] \sin \theta dv d\theta. \quad (23)
 \end{aligned}$$

From the above expression it clear that the magnetic field energy stored in the spherical configuration is inversely proportional to time, decreasing as the radius expands.

Similarly, the energy stored in the electric field is given from the following expression:

$$\begin{aligned}
 E_{el} &= \frac{2\pi}{8\pi} \int_0^\pi \int_0^R \frac{v^2}{(2\pi r^2 \sin \theta)^2} \left[(v \partial_v \Psi)^2 + \left(\Gamma^2 v \sqrt{c_0} \Psi \right)^2 \right] \times \\
 &\times r^2 \sin \theta dr d\theta \\
 &= \frac{1}{16\pi c t} \int_0^\pi \int_0^{v_0} \frac{1}{\sin^2 \theta} \left[(v \partial_v \Psi)^2 + \right. \\
 &+ \left. \left(\Gamma^2 v \sqrt{c_0} \Psi \right)^2 \right] \sin \theta dv d\theta. \quad (24)
 \end{aligned}$$

As the electric field is the θ and ϕ components of the magnetic field multiplied by the velocity, it follows a similar behaviour, with electric field energy being inversely proportional to time.

Thus, as the system expands it decreases. Electric and magnetic field energy contained within a sphere as a function of c_0 is shown in figure 6, where the solution for the Z ($c_1 = 0$) and N-models ($c_1 < 0$) is shown. We find that for smaller and larger values of c_0 the magnetic field energy is higher and has a minimum for intermediate c_0 . We remark that in the solutions we have normalised the maximum value of g and consequently Ψ to unity. Because of this, while the magnetic flux is the same in all solutions its energy content is related to how it is distributed in the sphere. In the case of a smaller sphere and large c_0 , all components of the magnetic field are large since they scale inversely with r . For spheres where v_0 approaches unity, while the radius is higher, g develops a sharp derivative at v_0 , leading to a strong B_θ component and energy content. On the contrary, the electric field energy has a monotonic dependence c_0 as its intensity is proportional to v , therefore for smaller spheres, in velocity space, its overall contribution is smaller, even though the magnetic field energy is higher.

4.2.2. Mass

The density profile of the plasmoid is related to the flux function Ψ , equations (17) and (21) multiplied by the prefactor $\Gamma^3 v^3 / r^3$ as demonstrated in equation (15). The two families of solutions we have studied here, for positive and negative c_1 have qualitatively different density profiles. For $c_1 > 0$, the minimum is located at the centre of the sphere ($r = 0$) and peaks close to the location of the maximum of Ψ with some modulation due to the Γ^3 prefactor

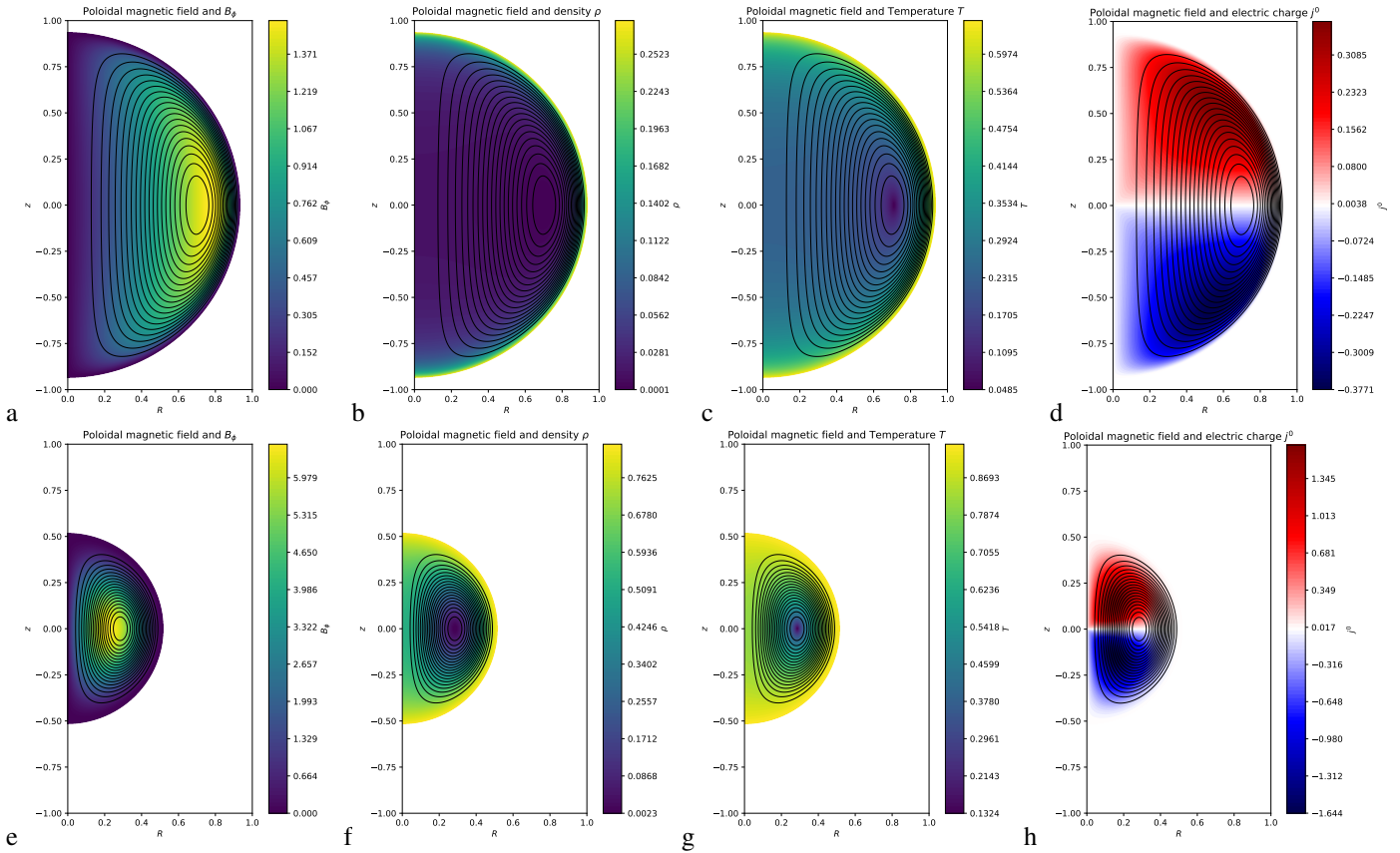


Fig. 5. Contour plots of the solutions with $c_0 = 10$ and $c_1 = -1.448$ (top row); and $c_0 = 100$ and $c_1 = -211.3$ (bottom row). The black contours correspond to the poloidal magnetic field lines, while in colour is plotted: the B_ϕ component of the magnetic field (panels a, e), the rest mass density ρ (panels b and f), the temperature T (panels c and g); and the electric charge density j^0 (panels d and h). As in the plots of Figure 5, the snapshot is taken at some time t , so that $r = 1$ corresponds to $v = 1$.

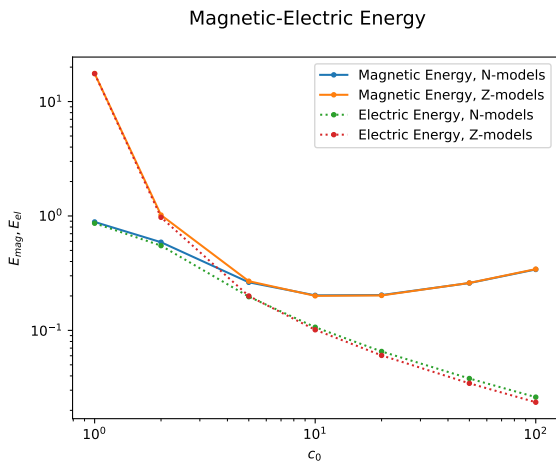


Fig. 6. The electric and magnetic energy for the the Z and N solutions as functions of c_0 .

that will push the maximum closer to the surface. On the contrary for $c_1 < 0$, the minimum is located close to the maximum of Ψ .

Let us first consider the rest mass contained within the expanding plasmoid. We integrate the rest mass density expression given by equation (15) within a sphere of given radius R , so that $R = cv_0 t$ at some time t , therefore corresponding to the physical location of the non-zero root of g . Accounting for the axial symmetry of the system, integration over ϕ provides a factor of

2π .

$$\begin{aligned}
 M &= 2\pi \int_0^\pi \int_0^R \left(\tilde{p}_0 + c_1 \frac{g(v) \sin^2 \theta}{16\pi^3} \right)^{3/4} Q(v, \theta)^{-3/4} \times \\
 &\quad \left(\frac{\Gamma(v)}{r} \right)^3 r^2 \sin \theta \, dr \, d\theta \\
 &= 2\pi \int_0^\pi \int_0^{R/(ct)} \left(\tilde{p}_0 + c_1 \frac{g(v) \sin^2 \theta}{16\pi^3} \right)^{3/4} Q(v, \theta)^{-3/4} \times \\
 &\quad \Gamma^3 \left(\frac{r}{ct} \right)^2 \sin \theta \, d\left(\frac{r}{ct} \right) \, d\theta \\
 &= 2\pi \int_0^\pi \int_0^{v_0} \left(\tilde{p}_0 + c_1 \frac{g(v) \sin^2 \theta}{16\pi^3} \right)^{3/4} Q(v, \theta)^{-3/4} \times \\
 &\quad \Gamma^3 v^2 \sin \theta \, dv \, d\theta. \tag{25}
 \end{aligned}$$

We confirm, as expected, that the rest mass contained within a spherical configuration does not evolve with time or the physical radius of the fluid, as the integral is on the v -space, where the solution does not evolve. However, the amount of mass contained inside the sphere, depends on the solution. In what follows we shall assume that the function Q is constant and sets the scale for the mass. Furthermore, the total mass is sensitive to the choice of the additive constant, \tilde{p}_0 . Here we make the following choices: for $c_1 > 0$, we set $\tilde{p}_0 = 0$, whereas for $c_1 < 0$ we choose the minimum acceptable value of \tilde{p}_0 so that the minimum of the density is exactly zero, thus $\tilde{p}_0 = -\frac{c_1}{16\pi^3}$. The resulting masses from the integration are shown in Figure 7. We notice that for higher absolute values of c_1 the mass is higher. We note that the assumption

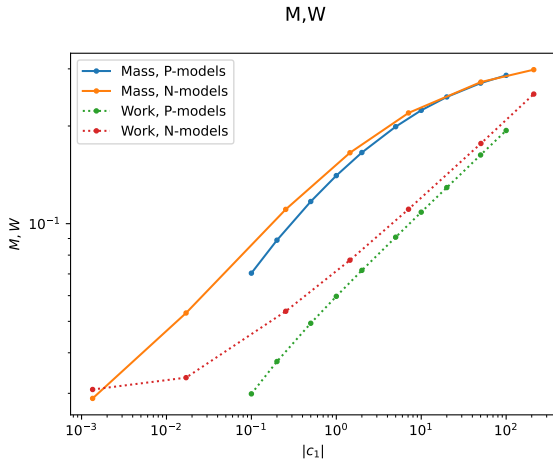


Fig. 7. The mass M and work W for the P and N solutions as functions of $|c_1|$. Note that while M and W are plotted on the same axis the units differ. Moreover, W evolves with time being inversely proportional to t .

of an additive constant affects the direct comparison of the mass: the P-type solutions have zero density on their surface, where the N-type ones have a non-zero density on their surfaces. To produce a reasonable comparison, if one considers the same density on the surface $v = v_0$ the P-type solutions have a higher mass load, compared to the N-type ones.

4.2.3. Thermal Pressure Work

Following a similar procedure as in the density we can evaluate the work W of the thermal pressure. It can be calculated through the integral of pdV . Upon integration for a sphere of radius R at time t , we obtain the following expression:

$$\begin{aligned} W &= 2\pi \int_0^\pi \int_0^R \left(\tilde{p}_0 + c_1 \frac{g(v) \sin^2 \theta}{16\pi^3} \right) \times \\ &\quad \left(\frac{\Gamma v}{r} \right)^4 r^2 \sin \theta \, dr \, d\theta \\ &= \frac{2\pi}{ct} \int_0^\pi \int_0^{v_0} \left(\tilde{p}_0 + c_1 \frac{g(v) \sin^2 \theta}{16\pi^3} \right) \times \\ &\quad \Gamma^4 v^2 \sin \theta \, dv \, d\theta. \end{aligned} \quad (26)$$

We notice that W is inversely proportional to t , signifying the expansion of the system. This work is associated to the spatial redistribution of the plasma mass and pressure as the system expands. We further note, that the thermal pressure on the the surface of the sphere decreases with time, thus as the system expands less work is done against the external medium. The results of this integration for various choices is shown in Figure 7, with the dotted lines.

4.2.4. Temperature

Given the relation between the density and the pressure we can evaluate the temperature of the plasmoid, through the relation $T = \frac{m_p}{k_B \rho}$, where m is the particle mass and k_B is the Boltzmann constant. Therefore, the temperature is given by the form:

$$T = \frac{m \tilde{p} \Gamma v}{k_B \tilde{\rho} r} = \frac{m \tilde{p} \Gamma}{k_B \tilde{\rho} ct} \quad (27)$$

Therefore, the local temperature is inversely proportional to t , with the expansion of the system leading to cooling.

As $\tilde{\rho}$ and $\tilde{\rho}$ are related to each other through Q , we are going to follow the assumption of a constant value of $Q(v, \theta)$ in the evaluation of the temperature, as we have already chosen in the calculation of mass through the density. Therefore, we expect a temperature profile for the spherical structure that decreases inversely proportionally with time.

For positive values of c_1 the maximum value of the temperature coincides approximately with the maximum of the flux function Ψ , while it is cooler at the boundaries of the sphere and the axis, Figure 4 panels c and g. For negative values of c_1 the minimum of the temperature occurs close to the maximum of Ψ , while the surroundings are hotter as illustrated in Figure 5 panels c and g. For the normalisation values assumed here, see the caption of Table 1, and assuming a proton-electron plasma the units of the temperature correspond to 10^{11} K.

5. Astrophysical implications

The solutions derived here provide a framework for the study of astrophysical systems of relativistically expanding configurations of magnetised plasma. It has been proposed that such structures may arise from magnetars expelling mass-loaded magnetic structures, which are associated to magnetar flares (Thompson & Duncan 2001; Lyutikov 2006), and possibly to FRBs (Bransgrove et al. 2025).

5.1. Magnetar flares

Magnetic fields of magnetars are highly active and evolve due to MHD effects in the crust, such as Hall drift (Goldreich & Reisenegger 1992; Pons et al. 2009; Gourgouliatos et al. 2016; Kojima et al. 2021; Igoshev et al. 2021) and plastic flows (Levin & Lyutikov 2012; Lyutikov 2015; Lander 2016; Gourgouliatos & Lander 2021); and the core due to ambipolar diffusion and superconducting magnetic field evolution (Graber et al. 2015; Passamonti et al. 2017a,b; Igoshev & Hollerbach 2023; Skiathas & Gourgouliatos 2024; Igoshev et al. 2025). These effects lead to the formation of multipolar magnetic structures in the lower magnetosphere and may release them to the magnetosphere. Once an arcade forms in the magnetosphere, it is possible through high twist to become unstable (Parfrey et al. 2013; Ntotsikas & Gourgouliatos 2025) and disconnect from the stellar magnetic field (Lander et al. 2024; Bransgrove et al. 2025). Such configurations evolve dynamically and give rise to a magnetar flare Figure 8. Magnetar flares are rare explosive events that occur in magnetars. A flare can release immerse amounts of energy reaching 10^{46} erg in the form of X-rays, shining within a fraction of a second. Moreover, flare ejecta expel masses reaching $10^{24} - 10^{26}$ g (Gaensler et al. 2005; Granot et al. 2006), which are subsequently powering scaled-down version of kilonovae through r-process radioactive decay (Cehula et al. 2024).

In the model developed here, the relative content of the spherical configuration in mass, thermal pressure, magnetic and electric energy, temperature profile and the maximum Lorentz factor attained are all related through the choices of the parameters c_0 and c_1 . Assuming that a blob has a radius of 1km (10^5 cm) and the maximum value of the magnetic flux corresponds to 10^{25} G cm 2 , so that the magnetic field scales with 10^{15} G, the magnetic and electric field energies E_{mag} and E_{el} range from 10^{44} erg to 10^{46} erg. The pressure work W ranges from 10^{43} erg to 10^{45} erg and the temperature is at a level of 10^{11} . We note that the temperature and energetics evolve with time as the plasmoid expands, with the decrease in electromagnetic and thermal energy

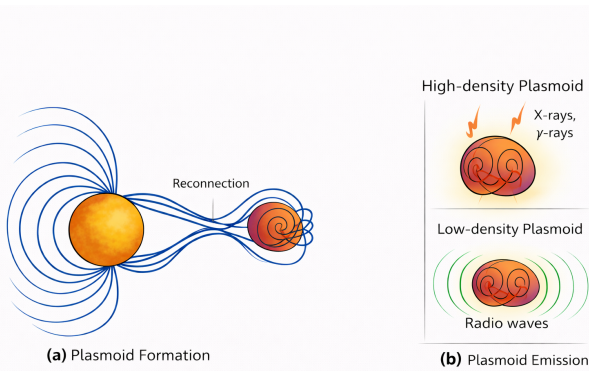


Fig. 8. Schematic illustration of plasmoid formation and emission regimes associated with the different families of self-similar solutions. (a) Magnetic reconnection in the magnetar magnetosphere leads to the formation of a magnetically confined plasmoid embedded within the closed field region. (b) Emission properties of plasmoids corresponding to different mass-loading regimes: P-type solutions (overdense) predominantly emit high-energy radiation (X-rays and γ -rays), whereas Z- and N-type solutions (underdense, magnetically dominated configurations) correspond to low-density plasmoids capable of producing coherent radio emission.

of the sphere to be related to the work done against the external medium that the sphere is expanding. The mass load M ranges from 10^{24} g to 10^{25} g and does not evolve with time.

5.1.1. Giant flare energetics

Here, magnetar giant flares are interpreted as large-scale, relativistic magnetic reconfigurations described by self-similar, axisymmetric MHD solutions with finite mass loading. For all explored solution families (Z, P, and N), the energy budget at early times is dominated by the electromagnetic component, while the kinetic and thermal contributions depend on the mass-loading and the pressure term which are quantified through parameter c_1 . This is a necessary condition for producing a bright, rapidly varying high-energy spike, since a kinetic- or thermal-energy-dominated outflow would radiate inefficiently at X-ray and γ -ray energies and primarily power delayed, shock-driven emission. The electromagnetic dominance of the early-time evolution is therefore consistent with the observation that the prompt hard X-ray/ γ -ray spike contains the majority of the radiated energy in magnetar giant flares (e.g. Hurley et al. 2005; Palmer et al. 2005).

An immediate observational implication is that giant flares may exhibit significant diversity in their late-time signatures despite comparable prompt luminosities. Solutions with larger mass loading (P-type) predict enhanced interaction between the ejecta and the surrounding medium, potentially giving rise to detectable radio afterglows or nebular disturbances, as observed following the 2004 flare of SGR 1806–20 (Gaensler et al. 2005). In contrast, low-mass solutions (Z- and N-type) correspond to clean flares, in which little kinetic energy is available to power long-lived afterglow emission, consistent with the weaker radio signatures of SGR 1900+14 (Frail et al. 1999).

5.1.2. Timescales and light-curve morphology

The self-similar expansion fixes the characteristic radial scale of the system to

$$r(t) = cv_0 t, \quad (28)$$

with v_0 of order unity. Dissipation is expected to occur preferentially near the outer boundary of the expanding structure, where strong current sheets and pressure gradients develop. This naturally leads to sub millisecond-scale rise times for the initial hard X-ray/ γ -ray spike, consistent with the observed rise times of Galactic giant flares (Palmer et al. 2005; Hurley et al. 2005).

The model predicts temporally asymmetric light curves, characterized by a very rapid rise phase followed by a longer decay. The rise time reflects localized dissipation at the expanding boundary, whereas the decay traces the subsequent global magnetic reconfiguration of the system. Since these timescales depend primarily on the expansion speed rather than on the total energy release, similar rise times are expected across giant flares of different luminosities. While the presence of strong currents and discontinuities lead to dissipation and current driven instabilities, a detailed study is required to confirm and follow in detail the development of these effects.

5.1.3. Angular structure and anisotropy

The meridional structure of the solution leads to highly anisotropic profiles with magnetic field, pressure and mass loading to be different on the equator and the poles. Consequently, the emitted radiation is expected to be anisotropic, with the apparent energy of a flare depending on the observer's viewing angle relative to the magnetic field symmetry axis.

Such anisotropy provides a natural explanation for the wide dispersion in inferred isotropic-equivalent energies among observed giant flares (Hurley et al. 1999), without requiring intrinsic energy releases spanning several orders of magnitude.

5.1.4. Mass loading and flare diversity

The explored parameter space spans ejecta masses ranging from effectively negligible values (Z-type solutions) up to $\sim 10^{25}$ – 10^{26} g. This range is consistent with estimates of the ejecta mass inferred from modelling the radio afterglow of SGR 1806–20 (Gaensler et al. 2005; Granot et al. 2006). Low-mass events, associated with Z- and N-type solutions, correspond to predominantly magnetospheric reconfigurations with minimal baryon contamination. These events are expected to produce sharp, luminous high-energy spikes and weak or undetectable afterglows.

In contrast, P-type solutions involve substantial mass loading, potentially including baryonic material originating from the stellar crust or inner magnetosphere (Thompson & Duncan 2001; Bransgrove et al. 2025). Such events are expected to exhibit stronger interaction with the ambient medium, leading to detectable radio afterglows or long-lived nebular emission.

5.1.5. Spectral and polarization signatures

As the system expands self-similarly, the magnetic field strength decreases rapidly with radius, implying fast spectral evolution of the emitted radiation. The model predicts an initially hard spectrum during the prompt spike, followed by rapid hard-to-soft evolution on millisecond timescales, in agreement with observed giant flare spectra (Feroci et al. 2001; Olive et al. 2004).

Because the magnetic field remains globally ordered during the early stages of the expansion, the prompt emission is expected to be highly linearly polarized, with a relatively stable polarization angle during the rise phase. This is consistent with expectations for magnetically dominated emission regions (Lyutikov 2006). Significant depolarization may occur only at later times, once magnetic reconnection and dissipation disrupt the large-scale field structure.

5.2. Fast radio bursts

Within the present framework, FRBs are interpreted as the coherent radio counterparts of magnetically dominated explosions with low baryon loading Lyubarsky (2021). While the total energy release and large-scale dynamics may resemble those of magnetar giant flares, the conditions required for efficient coherent emission impose strong constraints on the ejecta mass and magnetization. In particular, FRB production is favoured in solutions where the electromagnetic energy dominates over both kinetic and thermal components throughout the early expansion (Lyutikov 2017; Beloborodov 2017).

In heavily mass-loaded explosions, such as P-type solutions, the inertia of the ejecta and the rapid formation of a strong compression shock suppress coherent emission by reducing the magnetization and increasing the plasma frequency. These events are therefore expected to produce luminous high-energy flares but weak or absent radio bursts. In contrast, Z- and N-type solutions correspond to minimally mass-loaded outflows in which the plasma remains highly magnetized and optically thin, allowing coherent radio emission to escape. This qualitative distinction is consistent with the observed diversity of magnetar activity, including radio-quiet giant flares and radio-loud but energetically modest bursts (Kaspi & Beloborodov 2017; Mereghetti et al. 2020).

The self-similar expansion naturally leads to the formation of strong current sheets and charge-starved regions near the expanding boundary of the magnetized structure. In such regions, large-amplitude electromagnetic disturbances can be generated on millisecond timescales, providing favourable conditions for coherent curvature radiation or synchrotron maser emission at relativistic shocks (Lyubarsky 2014; Plotnikov & Sironi 2019). The characteristic duration of the resulting radio burst is set by the causal timescale $t \sim r/c$, consistent with the millisecond durations of observed FRBs.

An important prediction of the model is that FRBs need not be associated with the most energetic magnetar flares. Instead, they preferentially accompany low-mass explosions in which a large fraction of the released energy remains in electromagnetic form rather than being degraded into kinetic energy at shocks (Lyutikov 2022). This provides a natural explanation for the observed association of FRBs with magnetars (Popov & Postnov 2013), including the detection of a bright radio emission coincident with an X-ray flare from SGR 1935+2154 (Cameron et al. 2005; Bochenek et al. 2020; CHIME/FRB Collaboration et al. 2020), as well as the absence of FRBs during the most extreme giant flares.

6. Conclusions

We have presented a class of self-similar, axisymmetric MHD solutions describing relativistic, magnetically dominated explosions with mass loading, motivated by energetic transient phenomena in magnetar magnetospheres. The solutions encompass

a broad range of behaviours, characterised by different degrees of baryon loading and pressure support, while remaining analytically tractable.

A central result of this work is that the early-time evolution of these explosions is generically dominated by electromagnetic energy, with kinetic and thermal components becoming important only as a consequence of mass loading and interaction with the external medium. This regime naturally produces rapid, high-energy emission on millisecond timescales, followed by a longer decay associated with magnetic energy depletion and eventual deceleration by a compression shock. The resulting light curves are strongly asymmetric, with rise times controlled primarily by the expansion speed and geometry rather than by the total energy release.

Applied to magnetar giant flares, the model reproduces key observational properties, including sub-millisecond rise times, hard prompt spectra, low radiative efficiencies, and the presence or absence of afterglow emission depending on the ejecta mass. Heavily mass-loaded solutions are associated with efficient energy transfer to shocks and long-lived radio nebulae, while lightly loaded solutions correspond to “clean” magnetospheric reconfigurations with weak or undetectable afterglows.

In this context, FRBs arise naturally from low-mass, highly magnetized explosions in which coherent radio emission can escape before significant baryon loading or shock formation suppresses it. The model therefore predicts that FRBs need not accompany the most energetic magnetar flares, but instead preferentially occur in events where the electromagnetic energy remains dominant throughout the early expansion. This provides a unified explanation for the observed diversity of magnetar activity, including radio-quiet giant flares, radio-loud but energetically modest bursts, and rare events exhibiting both high-energy and radio emission.

The present model is based on a semi-analytical approach, considering ideal MHD, axial symmetry and self-similarity. These simplifications allow the consistent formation of models and the thorough exploration of the parameter space that illustrates the main qualitative characteristics. However, some of the key effects that are associated to observable properties of magnetar flares and FRBs require the relaxation of these idealisations. Namely, the expansion of a spherical magnetised plasmoid, as it propagates away from the neutron star, is not guaranteed to remain self-similar. Moreover, these spherical large-scale plasmoids may deviate from the spherical shape and axial symmetry. Finally, resistive instabilities and the possible formation of shocks due to the interaction of the mass with the external medium will shape the radiative properties of the plasmoid. These deviations can be traced with a numerical simulation that will allow to determine the limitations of the approach made here and their consequences for the observables.

Overall, the results presented here demonstrate that a single, physically motivated class of magnetically dominated, mass-loaded explosions can account for a wide range of observed transient phenomena associated with magnetars. By explicitly linking the dynamics to a small number of physical parameters, the model provides a coherent framework for interpreting present observations and for guiding future multi-wavelength and polarization measurements of magnetar-driven transients.

Data availability

The datasets generated during the current study are available from the author upon reasonable request.

Acknowledgements. The author acknowledges funding from grant FK 81641 "Theoretical and Computational Astrophysics", ELKE. This work was supported by computational time granted by the National Infrastructures for Research and Technology S.A. (GRNET S.A.) in the National HPC facility - ARIS - under project ID pr017008/simnstar2.

References

Barkov, M. V., Sharma, P., Gourgouliatos, K. N., & Lyutikov, M. 2022, *ApJ*, 934, 140

Beloborodov, A. M. 2017, *ApJ*, 843, L26

Beniamini, P., Wadiasingh, Z., Trigg, A., et al. 2025, *ApJ*, 980, 211

Bochenek, C. D., Ravi, V., Belov, K. V., et al. 2020, *Nature*, 587, 59

Bransgrove, A., Beloborodov, A. M., & Levin, Y. 2025, arXiv e-prints, arXiv:2508.13419

Cameron, P. B., Chandra, P., Ray, A., et al. 2005, *Nature*, 434, 1112

Cehula, J., Thompson, T. A., & Metzger, B. D. 2024, *MNRAS*, 528, 5323

Chandrasekhar, S. & Kendall, P. C. 1957, *ApJ*, 126, 457

CHIME/FRB Collaboration, Andersen, B. C., Bandura, K. M., et al. 2020, *Nature*, 587, 54

Demidov, I. & Lyubarsky, Y. 2023, *MNRAS*, 518, 810

Feroci, M., Hurley, K., Duncan, R. C., & Thompson, C. 2001, *ApJ*, 549, 1021

Frail, D. A., Kulkarni, S. R., & Bloom, J. S. 1999, *Nature*, 398, 127

Gaensler, B. M., Kouveliotou, C., Gelfand, J. D., et al. 2005, *Nature*, 434, 1104

Goldreich, P. & Reisenegger, A. 1992, *ApJ*, 395, 250

Gourgouliatos, K. N., Braithwaite, J., & Lyutikov, M. 2010, *MNRAS*, 409, 1660

Gourgouliatos, K. N. & Lander, S. K. 2021, *MNRAS*, 506, 3578

Gourgouliatos, K. N. & Lynden-Bell, D. 2008, *MNRAS*, 391, 268

Gourgouliatos, K. N. & Lyutikov, M. 2012, *MNRAS*, 420, 505

Gourgouliatos, K. N. & Vlahakis, N. 2010, *Geophysical and Astrophysical Fluid Dynamics*, 104, 431

Gourgouliatos, K. N., Wood, T. S., & Hollerbach, R. 2016, *Proceedings of the National Academy of Science*, 113, 3944

Graber, V., Andersson, N., Glampedakis, K., & Lander, S. K. 2015, *MNRAS*, 453, 671

Granot, J., Ramirez-Ruiz, E., Taylor, G. B., et al. 2006, *ApJ*, 638, 391

Harris, C. R., Millman, K. J., van der Walt, S. J., et al. 2020, *Nature*, 585, 357

Hurley, K., Boggs, S. E., Smith, D. M., et al. 2005, *Nature*, 434, 1098

Hurley, K., Cline, T., Mazets, E., et al. 1999, *Nature*, 397, 41

Igoshev, A., Moraga, N. A., Reisenegger, A., Skene, C. S., & Hollerbach, R. 2025, arXiv e-prints, arXiv:2512.13408

Igoshev, A. P. & Hollerbach, R. 2023, *MNRAS*, 518, 821

Igoshev, A. P., Hollerbach, R., Wood, T., & Gourgouliatos, K. N. 2021, *Nature Astronomy*, 5, 145

Kaspi, V. M. & Beloborodov, A. M. 2017, *ARA&A*, 55, 261

Kojima, Y., Kisaka, S., & Fujisawa, K. 2021, *MNRAS*, 502, 2097

Lander, S. K. 2016, *ApJ*, 824, L21

Lander, S. K., Gourgouliatos, K. N., Wadiasingh, Z., & Antonopoulou, D. 2024, arXiv e-prints, arXiv:2411.08020

Levin, Y. & Lyutikov, M. 2012, *MNRAS*, 427, 1574

Lorimer, D. R., Bailes, M., McLaughlin, M. A., Narkevic, D. J., & Crawford, F. 2007, *Science*, 318, 777

Lyubarsky, Y. 2014, *MNRAS*, 442, L9

Lyubarsky, Y. 2021, *Universe*, 7, 56

Lyutikov, M. 2006, *MNRAS*, 367, 1594

Lyutikov, M. 2015, *MNRAS*, 447, 1407

Lyutikov, M. 2017, *ApJ*, 838, L13

Lyutikov, M. 2022, *MNRAS*, 509, 2689

Marcote, B., Nimmo, K., Hessels, J. W. T., et al. 2020, *Nature*, 577, 190

Mereghetti, S., Savchenko, V., Ferrigno, C., et al. 2020, *ApJ*, 898, L29

Metzger, B. D., Margalit, B., & Sironi, L. 2019, *MNRAS*, 485, 4091

Ntotsikas, D. & Gourgouliatos, K. N. 2025, *A&A*, 700, A103

Olive, J.-F., Hurley, K., Sakamoto, T., et al. 2004, *ApJ*, 616, 1148

Palmer, D. M., Barthelmy, S., Gehrels, N., et al. 2005, *Nature*, 434, 1107

Parfrey, K., Beloborodov, A. M., & Hui, L. 2013, *ApJ*, 774, 92

Passamonti, A., Akgün, T., Pons, J. A., & Miralles, J. A. 2017a, *MNRAS*, 469, 4979

Passamonti, A., Akgün, T., Pons, J. A., & Miralles, J. A. 2017b, *MNRAS*, 465, 3416

Patel, A., Metzger, B. D., Cehula, J., et al. 2025, *ApJ*, 984, L29

Petroff, E., Hessels, J. W. T., & Lorimer, D. R. 2019, *A&A Rev.*, 27, 4

Plotnikov, I. & Sironi, L. 2019, *MNRAS*, 485, 3816

Pons, J. A., Miralles, J. A., & Geppert, U. 2009, *A&A*, 496, 207

Popov, S. B. & Postnov, K. A. 2013, arXiv e-prints, arXiv:1307.4924

Prendergast, K. H. 2005, *MNRAS*, 359, 725

Skiathas, D. & Gourgouliatos, K. N. 2024, *MNRAS*, 528, 5178

Tavani, M., Casentini, C., Ursi, A., et al. 2021, *Nature Astronomy*, 5, 401

Thompson, C. & Duncan, R. C. 1995, *MNRAS*, 275, 255

Thompson, C. & Duncan, R. C. 2001, *ApJ*, 561, 980

Trigg, A. C., Stewart, R., Van Kooten, A., et al. 2025, *A&A*, 694, A323

Virtanen, P., Gommers, R., Oliphant, T. E., et al. 2020, *Nature Methods*, 17, 261

Wadiasingh, Z. & Timokhin, A. 2019, *ApJ*, 879, 4

Yuan, Y., Beloborodov, A. M., Chen, A. Y., & Levin, Y. 2020, *ApJ*, 900, L21